CRYSTAL GROWTH & DESIGN

Article

pubs.acs.org/crystal

Modeling Nucleation, Growth, and Ostwald Ripening in Crystallization Processes: A Comparison between Population Balance and Kinetic Rate Equation

Thomas Vetter,[†] Martin Iggland,[†] David R. Ochsenbein,[‡] Flurin S. Hänseler,[†,§] and Marco Mazzotti*[,†]

[†]Institute of Process Engineering, ETH Zurich, Sonneggstrasse 3, CH-8092 Zurich, Switzerland

[‡]Automatic Control Laboratory, ETH Zurich, Physikstrasse 3, CH-8092 Zurich, Switzerland

Supporting Information

ABSTRACT: In this work, we investigate a comprehensive model describing nucleation, growth and Ostwald ripening based on the kinetic rate equation and compare it to commonly used population balance equation models that either describe nucleation and crystal growth or crystal growth and Ostwald ripening. The kinetic rate equation gives a microscopic description of crystallization, i.e., the process is seen as an attachment and detachment of crystals of different sizes to and from each other, thereby changing their size. A hybrid model is employed in which the discrete kinetic rate equation is used to describe the smallest particle sizes while a Fokker−Planck equation is used to approximate the kinetic rate equation at larger particle sizes. This allows us to cover crystals in a size range starting from a single molecule up to macroscopic particle sizes and to solve the model numerically with reasonable computational effort and great accuracy. We show that the model based on the kinetic rate equation describes the processes of nucleation, crystal growth, and Ostwald ripening accurately in a single, continuous model. This is set in contrast with classical population balance equation models that require, due to their underlying assumptions, separation of the process of nucleation from the process of Ostwald ripening. We compare the results of the two models for different sets of parameters (such as different solubilities, surface tensions, initial supersaturations, and seed distributions). Using these results, we assess the advantages and disadvantages of models based on the kinetic rate equation in comparison to models employing a population balance equation.

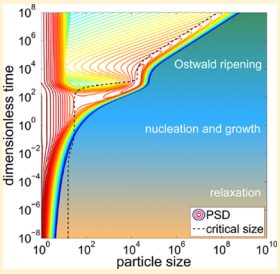

1. INTRODUCTION

In crystallization processes, a solute is transferred from a liquid or vapor to a solid phase due to a difference in chemical potential between the two phases. This process is usually described as a combination of several mechanisms: the formation of the new phase (nucleation), growth of crystals, and secondary effects such as agglomeration and breakage. The combination of these effects determines the evolution of the particle size distribution (PSD) until the supersaturation of the solution is depleted. When starting from an initially solid-free system, nucleation is dominant at the beginning of the process, when typically the difference in chemical potential between solution and the solid phase, or supersaturation, is high. Crystal growth becomes significant as soon as crystals are present in the suspension and will dominate the decrease of supersaturation after some time. Crystal breakage and agglomeration on the other hand are dominated by particle−particle interactions, reactor design, and hydrodynamics and only have an influence on the size and structure of particles but do not directly affect the solution concentration. After the depletion of supersaturation, a mechanism known as Ostwald ripening[1,2] (also referred to as coarsening, aging, or simply ripening) takes over and further influences the evolution of the particle size distribution, while breakage and agglomeration can continue to act on the crystals.

Two established classes of models have been frequently used to describe the governing mechanisms of these processes in detail; the goal of this work is to compare them and to identify similarities and differences between the two: population balance equation (PBE) models[3−5] and models based on the kinetic rate equation (KRE).[6]

PBE models applied to crystallization processes have been widely described in the literature, accounting for various combinations of the mechanisms described above. The simplest models describe only growth processes.[7,8] For unseeded crystallizations, nucleation is included using nucleation rates based on classical nucleation theory,[9−12] typically expressed as functions of the mechanisms considered (primary or secondary; homogeneous or heterogeneous).[13,14] The secondary mechanisms breakage and agglomeration have been the subject of several works.[3,15−19] The size dependence of solubility, which governs Ostwald ripening, has been considered and modeled by several authors,[20−25] as reviewed recently.[26]

Though very powerful, PBE models cannot describe Ostwald ripening and nucleation simultaneously. This is because the nucleation models assume a constant critical size, while the Ostwald ripening models require the critical size to be a function of the supersaturation. This situation is unsatisfactory, both conceptually and practically, since the basic mechanisms

Received: July 15, 2013
Revised: August 30, 2013
Published: October 1, 2013

   dx.doi.org/10.1021/cg4010714 | Cryst. Growth Des. 2013, 13, 4890−4905

behind nucleation, growth, and ripening are the same and, in some applications, for example, precipitation of multiple polymorphs,[27] nucleation and growth, or ripening, occur for different solid phases at the same time. A model that includes all these steps has been presented by Kashchiev,[6] based on monomolecular interactions between the solution and the solid phase. This model has been used to describe nucleation, growth, and ripening of silica polymorphs from a geological perspective[27] and in semiconductor nanocrystals.[28] Other models have been presented that cover all three stages of crystallization, but they suffer from limitations such as the use of simplified nucleation models[29−33] or the use of different model equations for each stage.[34−36]

In this work, we will first review the important aspects of the models used (section 2). We use dimensionless formulations to identify key parameters in both models (section 2.3) and then investigate the influence of these parameters on the kinetics of nucleation, crystal growth, and Ostwald ripening in seeded and unseeded processes at constant and varying supersaturation (section 3). Presenting these different types of simulations allows focusing on each kinetic phenomenon separately, so that the consistency of the PBE and KRE models can be thoroughly compared and differences and similarities can be highlighted. In the final part of the Results section, simulations in which nucleation, crystal growth, and Ostwald ripening are modeled within a continuous framework (based on the kinetic rate equation) are presented. We then define characteristic times for nucleation and the start of Ostwald ripening, and their dependence on key model parameters is investigated.

2. MODELING OF THE CRYSTALLIZATION PROCESS

In the following, we will review the current status of both population balance equation and kinetic rate equation models in relation to the description of nucleation, growth, and ripening. The aim of this section is not to give the reader a complete overview of the subject but to introduce the necessary background and to put our investigation in its proper context.

In both models, it is assumed that crystals can be described by a single characteristic length and that the surface tension between a crystal and its surrounding liquid can be represented by a single value. Although these are both obvious simplifications for faceted crystals, we will stick to this description for the sake of simplicity. A volume shape factor allows us to account for different shapes that can be described by one characteristic length, for example, cubes, spheres, etc. In this work, we will consider spherical crystals with a characteristic diameter and number of molecules n. For an easier comparison between the two models, we use the number of molecules as the size coordinate in both. From a physical point of view, n assumes integer values only, and so it is treated in the KRE model. However, whenever convenient, particularly in the PBE model, we treat the number of molecules in a particle as a continuous variable called $\tilde{n}$.

2.1. Population Balance Equation Model. To model populations of crystals, the population balance equation framework has been used extensively.[5] In this paper, we will focus on the interplay of nucleation, crystal growth, and Ostwald ripening, so agglomeration and breakage effects are not modeled for simplicity. The population balance equation for a well-mixed batch reactor then reads as

$$\frac{\partial f}{\partial t} + \frac{\partial (vf)}{\partial \tilde{n}} = J\delta(\tilde{n} - \tilde{n}_*) \tag{1}$$

where f is the number density distribution of the crystals in the reactor, t is the time, and v is the (size-dependent) rate of crystal growth. By formulating the nucleation term on the right-hand side (rhs) of eq 1 in this way, it is assumed that nuclei appear exclusively at the critical size, $\tilde{n}_*$, with a nucleation rate J ($\delta(\tilde{n} - \tilde{n}_*)$ being the Dirac delta function). The assumption that nuclei emerge at a single size is made in the vast majority of all publications that use population balance equation models and take nucleation into account.[37−40]

Supplying appropriate initial and boundary conditions completes the formulation of eq 1 and allows accounting for seeded crystallization processes. The PBE is coupled with a mass balance for the liquid phase, written as

$$\frac{\mathrm{d}c}{\mathrm{d}t} = -\frac{1}{N_\mathrm{A}}\frac{\mathrm{d}}{\mathrm{d}t}\int_0^\infty \tilde{n} f \,\mathrm{d}\tilde{n} \tag{2}$$

where N_A is the Avogadro number. The formulation of eq 2 is again completed by an appropriate initial condition.

Considering how eq 1 is formulated, it is clear that sub- and supercritical crystals are not treated equally. While the description of supercritical crystals is continuous, crystal nuclei appear directly at the critical size, without considering their evolution up to that point, that is, the "growth" phase of the subcritical crystals is not described. Treating sub- and supercritical crystals in this way makes sense if the subcritical size range is small and of lesser interest compared with the supercritical size range. Although simplified, many researchers successfully use such PBE models to describe crystallization processes where nucleation, growth, or both occur.[11,12,14,18,41−43] Typically in these cases, solubility is considered to be size-independent, and the growth rate is defined as proportional to a power of the difference between actual concentration and solubility, that is, $v \propto (c - c_\infty)^b$.

However, it is mandatory to accurately describe subcritical crystals when Ostwald ripening is considered, because this phenomenon is indeed a consequence of the opposite behavior of subcritical crystals, which dissolve, and supercritical crystals, which grow.[26] This is accomplished by using a size-dependent growth rate incorporating the Gibbs−Thomson relationship.[7] In a general form, such a growth rate can be written as

$$v(\tilde{n}) = k\tilde{n}^a N_\mathrm{A}{}^b\left(c - c_\infty \exp\left(\frac{\alpha}{\tilde{n}^{1/3}}\right)\right)^b \propto (c - c_*(\tilde{n}))^b \tag{3}$$

where k is a rate constant, α is the dimensionless capillary length (see Appendix A in the Supporting Information for a derivation), a and b are constants that depend on the growth mechanism, c_∞ is the bulk solubility (the solubility of an infinitely large particle), and c_* is the size-dependent solubility of a particle of size $\tilde{n}$. This expression results in a growth rate that is positive for supercritical crystals and negative for subcritical crystals (note that b is an odd integer). Equation 3 can be used to approximate analytically derived expressions for different growth rate mechanisms (e.g., diffusion limited growth, 2D nucleation, or spiral growth) by changing the parameters k, a, and b.

Unfortunately, the growth rate expression in eq 3 cannot be reconciled with nucleation as written in eq 1. This is because nuclei formed at a finite critical size consume supersaturation (cf. eq 2), which leads to an increase in the critical size (see Appendix A in the Supporting Information). As a consequence, nuclei formed at the critical size at one point in time would start to dissolve immediately thereafter, and no stable, supercritical crystals could ever be formed.

One approach to overcome this difficulty is that of allowing the particle size to change randomly (see, for example, Ramkrishna,[5] Chapter 2.10). This approach involves first describing the random component of the particle evolution using a stochastic equation, which includes a term that varies randomly with time with a weight that is a function of time and particle size. Then this can be incorporated into the PBE using Ito's calculus,[44] thus obtaining a PBE that contains the same terms as eq 1 plus a second-order derivative of the particle size distribution f multiplied by a time- and size-dependent coefficient. This last term accounts for random changes in particle size by introducing a dispersion effect, typical of second-order terms, along the internal coordinate $\tilde{n}$. In this way, particles can cross the critical size and grow beyond it, even when the size-dependent growth and nucleation terms introduced above alone would not allow for that. A detailed discussion of this approach, which is very rarely used, is beyond the scope of this work.

Another alternative often employed to resolve this inconsistency is to treat the different phases of the crystallization process using two separate models. When such an approach is used, nucleation and growth are separated from the Ostwald ripening regime by assuming that

dx.doi.org/10.1021/cg4010714 | Cryst. Growth Des. 2013, 13, 4890−4905

nucleation occurs at high supersaturation with a rate that depends on the (varying) supersaturation and that the solubility in that process phase can be considered size-independent. The only way to accomplish this and be consistent with the Gibbs–Thomson relationship is if $\alpha = 0$ so that the critical size becomes zero and supersaturation-independent as well (see Appendix A in the Supporting Information).[37] However, one also finds the use of nonzero (but negligibly small) nuclei sizes in the literature[19,39] and of supersaturation-dependent nuclei sizes,[38] which is inconsistent with the Gibbs–Thomson relationship but often found accurate enough for the purposes of these studies.

Following classical nucleation theory, the nucleation rate J is typically described in a form similar to

$$J = K_1 S \exp\left(-\frac{K_2}{\ln^2 S}\right) \tag{4}$$

where $S = c/c_\infty$ is the supersaturation, K_1 is a parameter determined by the kinetic aspects of nucleation, whose various expressions can be found in the literature,[6,45,46] and K_2 is a parameter that depends purely on the thermodynamic properties of the system. According to classical nucleation theory, the argument of the exponential function in the last equation is proportional to the work to form a crystal of critical size, $\Delta G(\tilde{n}_*)$, as given by

$$\frac{K_2}{\ln^2 S} = \frac{\Delta G(\tilde{n}_*) N_A}{RT} = \frac{\alpha^3}{2 \ln^2 S} \Rightarrow K_2 = \frac{\alpha^3}{2} \tag{5}$$

Despite its strong assumptions and its obvious inconsistencies, this simplified model delivers a sufficiently accurate description of the crystallization process before Ostwald ripening becomes dominant. Note that the time when Ostwald ripening becomes important depends on the crystallization kinetics, the size dependence of the solubility, the size distribution of the crystals, and the supersaturation in the crystallizer (see Iggland and Mazzotti[26] for a detailed parameter study). Arriving at an essentially arbitrary threshold supersaturation, the population of particles resulting from such a nucleation and crystal growth model is then fed to a model describing Ostwald ripening.[20,21,26] In this model, nucleation is assumed to be effectively absent due to a low remaining supersaturation (i.e., $J = 0$) so that the discontinuity at the critical size can be removed and the sub- and supercritical crystals can be described in a continuous fashion. Hence, in these models the proper description of the size dependence of solubility, the growth rate, and the supersaturation dependency of the critical size is restored. However, at which value of supersaturation the switch between the model describing nucleation and the model describing Ostwald ripening is made is not clearly defined. Therefore, a model that describes all stages (nucleation, growth, and Ostwald ripening) with the same model equations constitutes an appreciable improvement from a conceptual and practical point of view.

2.2. Model Based on the Kinetic Rate Equations. The kinetic rate equation model[6] describes particles based on attachment and detachment of single molecules or of clusters of molecules, according to the pseudo-reaction scheme

$$A_n + A_j \underset{h(n+j,n)}{\overset{g(n,j)}{\rightleftharpoons}} A_{n+j} \tag{6}$$

Here, A_n denotes a crystal of size n, $g(n,j)$ is the rate constant of the two-particle attachment "reaction" of a crystal of size n to a crystal of size j, and $h(n + j,n)$ is the rate constant of the one-particle detachment of a crystal of size j from a crystal of size $n + j$. It is noteworthy that the attachment reaction accounts for both crystal growth (when n or j is 1) and agglomeration, whereas the detachment reaction accounts for both dissolution (when n or j equals 1) and breakage. Nucleation is not described explicitly as in the PBE model but occurs naturally as a result of the interplay of the ensemble of reactions in eq 6, provided attachment and detachment rates are properly defined.

Equation 6 describes the evolution of sub- and supercritical crystals, accounting for all mechanisms, in a single model. The importance of this inclusion is evidenced by several recent findings. To make an example, a study about the formation of platinum nanoparticles highlighted that agglomeration of subcritical crystals plays an important role in nucleation.[47] For such cases, models formulated in the spirit of eq 6 would provide distinct advantages over models based on eq 1. The goal of the present study, however, is the union of nucleation, growth, and Ostwald ripening; because agglomeration and breakage are not a prerequisite for nucleation, they are neglected in the following for simplicity. This leaves us with the following equations for the concentration Z_n of particles of size n (as originally outlined by Szilard and implemented by Farkas[10]):

$$\frac{dZ_1}{dt} = 2h(2)Z_2 + \sum_{j=3}^{\infty} h(j)Z_j - 2g(1){Z_1}^2 - Z_1 \sum_{j=2}^{\infty} g(j)Z_j \tag{7a}$$

$$\frac{dZ_n}{dt} = g(n-1)Z_1 Z_{n-1} + h(n+1)Z_{n+1} - g(n)Z_1 Z_n - h(n)Z_n \quad \text{for} \quad n \geq 2 \tag{7b}$$

Note that Kashchiev[6] uses the terminology "master equation" for these deterministic equations, that is, a term that is typically used for similar but stochastic equations in material and electrochemical science (and related fields). In order avoid confusion, we instead use the term "kinetic rate equation" throughout this paper. Also note that the argument of the attachment and detachment rate constants, $g(n)$ and $h(n + 1)$, has been simplified to reflect that only monomer attachments and detachments are considered.

Regarding the functional form of both rates, we follow the treatment by Kashchiev.[6] For the attachment rate, this yields

$$g(n) = kn^a \tag{8}$$

where the values of k and a depend on the substance under consideration and on the rate-limiting mechanism in the attachment of solute molecules to the crystals. We use a value of $a = 1/3$ unless otherwise stated, which corresponds to attachment controlled by volume diffusion (see Kashchiev,[6] pages 141–143). An exemplary value of $k = 6.86 \times 10^{-18}$ m^3 s^{-1} is chosen for all simulations, which is a realistic choice for a typical organic substance; a derivation of these values from readily available substance properties can be found elsewhere.[6,46,48] We will show in section 2.3 that the choice of the k value can be made without loss of generality. Since the attachment rate is obviously proportional to the concentration of crystals containing a single molecule, it is implicitly dependent on the supersaturation.

The detachment frequency can be derived by letting the frequency of detachment and attachment for a crystal of exactly the critical size, n_*, be equal, since the driving force for either growth or dissolution vanishes at that crystal size;[6,48] therefore,

$$h(n) = g(n)Z_1^*(n) \tag{9}$$

where $Z_1^*(n)$ is the solubility of a crystal of size n, analogously to c_*.

Clearly, this type of discrete description of particles requires keeping track of a huge number of particle sizes if macroscopic particles are to be described. This model can be transformed into a continuous form (see, for example, Kashchiev[6]), in which the discrete particle size, n, and particle size distribution, Z_n, are replaced by their continuous counterparts, $\tilde{n}$ and $\tilde{Z}(\tilde{n})$:

$$\frac{\partial \tilde{Z}}{\partial t} + \frac{\partial}{\partial \tilde{n}}\left(v\tilde{Z} - \frac{1}{2}\frac{\partial (H\tilde{Z})}{\partial \tilde{n}}\right) = 0 \tag{10}$$

where v and H are the net growth rate and effective dispersion coefficient, respectively.

In this formulation, the net growth rate is given by

$$v(\tilde{n}) = g(\tilde{n})Z_1 - h(\tilde{n}) \tag{11}$$

and the effective dispersion coefficient by

$$H(\tilde{n}) = g(\tilde{n})Z_1 + h(\tilde{n}) \tag{12}$$

Substituting eqs 8 and 9 into eq 11 yields

$$v(\tilde{n}) = k\tilde{n}^a\left(Z_1 - Z_{1,\infty}\exp\left(\frac{\alpha}{\tilde{n}^{1/3}}\right)\right) = k\tilde{n}^a N_A\left(c - c_\infty \exp\left(\frac{\alpha}{\tilde{n}^{1/3}}\right)\right) \tag{13}$$

dx.doi.org/10.1021/cg4010714 | Cryst. Growth Des. 2013, 13, 4890–4905

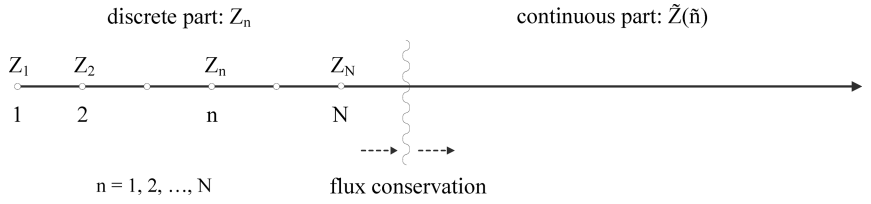

Figure 1. Combination of discrete and continuous descriptions of the crystal size domain. The two parts are connected at size $N + 1$. Details can be found in Appendix C of the Supporting Information.

Note that this is the same as the equation for the growth rate in the PBE model, eq 3, provided that the exponent b in eq 3 is chosen to be unity; hence the same symbol $v(\tilde{n})$ is used in both equations. The choice of $b = 1$ is a natural one when the "reactions" in eq 6 and the law of mass action are considered. Growth rate expressions that describe mechanisms such as birth and spread or spiral growth (see, for example, Ohara and Reid[49]) exhibit a different concentration dependence and could be modeled by adjusting the underlying reaction scheme. It is evident that different mechanisms could be rate controlling for different sizes of crystals; however, in order to not further complicate matters, we consider attachment and detachment kinetics to be controlled by volume diffusion over the whole size range.

The continuous formulation, which is derived from a Taylor expansion, introduces an error, particularly for small particles. Ozkan et al.[27] proposed to combine the advantages of both the discrete and continuous formulations by using a hybrid model. The idea behind this approach is illustrated in Figure 1. Up to a size N, the discrete formulation is used, and the continuous formulation is used for larger particles (in this work, $N = 50$). At the boundary between the two parts of the size domain, conservation of flux is enforced. The reader is referred to Appendix C in the Supporting Information, where the flux conservation and the numerical scheme to solve the Fokker–Planck equation are reported in detail.

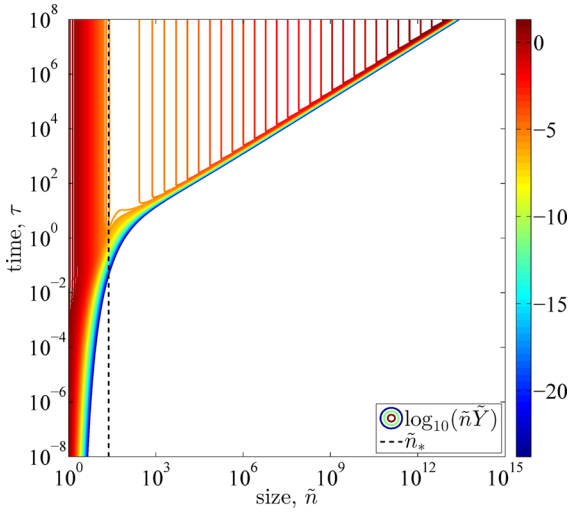

Figure 2. Unseeded simulations at constant supersaturation. Contour plot of the evolution of the volume-weighted PSD, $\tilde{n}\tilde{Y}$, obtained by solving the multiscale model based on the kinetic rate equation (note that the color scale is logarithmic). The data represented in this figure stem from a simulation with a supersaturation $S = 8$ and a dimensionless capillary length $\alpha = 6$.

Finally, it is worth noting that the continuous formulation of the KRE consists of an equation (eq 10) that contains a second-order derivative of the PSD like the formulation of the PBE accounting for random changes of the particle state (see section 2.1). Contrary to the mentioned PBE, the function H constituting the weight of the second-order term in eq 10 has a deterministic origin rather than a stochastic one.

2.3. Dimensionless Formulation of the KRE and the PBE Model. The model equations eqs 1, 2, 7, and 10 can be made dimensionless by introducing the quantities

$$Y_n = \frac{Z_n}{Z_{1,\infty}} \tag{14}$$

$$\tau = \frac{t}{t_0} \tag{15}$$

where t_0 is a reference time. The reference time is chosen to be

$$t_0 = (kZ_{1,\infty})^{-1} \tag{16}$$

These dimensionless variables are used to define dimensionless versions of the PBE as well as the discrete and continuous versions of the KRE (see Appendix B in the Supporting Information for details). For the PBE a dimensionless nucleation rate $\bar{\phi}$ can be defined, given by

$$\bar{\phi} = \frac{Jt_0}{Z_{1,\infty}} \tag{17}$$

Substituting eq 4 and taking the logarithm of both sides yields

$$\ln\left(\frac{\bar{\phi}}{S}\right) = \ln\left(\frac{t_0 K_1}{Z_{1,\infty}}\right) - \frac{K_2}{\ln^2 S} \tag{18}$$

Let us summarize the model parameters needed to carry out simulations with the KRE and the PBE models. The KRE model depends on only four parameters, namely, the nominal solubility, $Z_{1,\infty} = c_\infty N_A$, the attachment rate constant, k, both combined in t_0 as in eq 16, the constant exponent a (eq 8), and the constant α, related to the capillary length (see eq 3 in the Appendix, Supporting Information) . Introducing the dimensionless variables therefore allowed us to discover the scaling dependence between k and $Z_{1,\infty}$. For the PBE model, two more parameters are needed: K_1 and K_2, though K_2 was already shown to be proportional to α^3 (eq 5) and K_1 will be shown to be a function of α, k ,and $Z_{1,\infty}$ in section 3.1.

3. RESULTS

In order to compare the classical PBE model and the KRE model during different phases of a crystallization process (nucleation, crystal growth, and Ostwald ripening), we report simulations carried out using different parameter sets, thus investigating the influence of the dimensionless capillary length α and of the initial supersaturation as well as the effect of the presence of an initial population of crystals (seeded crystallization). To accomplish this, two different types of simulations are presented. In the first type of simulation (section 3.1), the supersaturation (and therefore the critical size) is kept constant. This has the advantage that Ostwald ripening is effectively avoided, thus allowing to us focus on the mechanisms of nucleation and crystal growth using simulations of unseeded and seeded processes, respectively. In the second type of simulation (section 3.2), we allow the supersaturation to vary during crystallization, thus permitting the investigation of Ostwald ripening. To this end, we report simulations of seeded processes starting from a saturated

dx.doi.org/10.1021/cg4010714 | Cryst. Growth Des. 2013, 13, 4890–4905

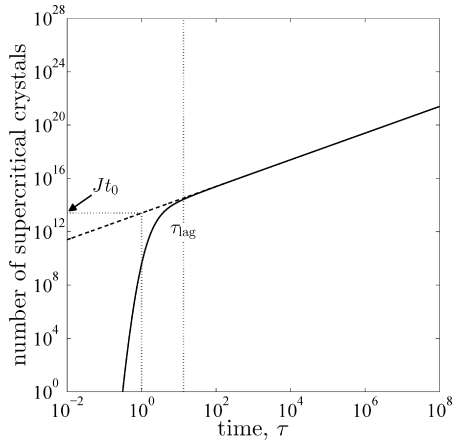

Figure 3. Unseeded simulations at constant supersaturation. Evolution of the number of supercritical crystals (simulation at supersaturation $S = 8$ and a dimensionless capillary length $\alpha = 6$) for the KRE model (solid line) and the classical PBE model (dashed line). The lag time, τ_{lag}, as defined in eq 20, is visualized with a dotted line. In this plot, the steady-state nucleation rate for both models is marked with an arrow on the ordinate.

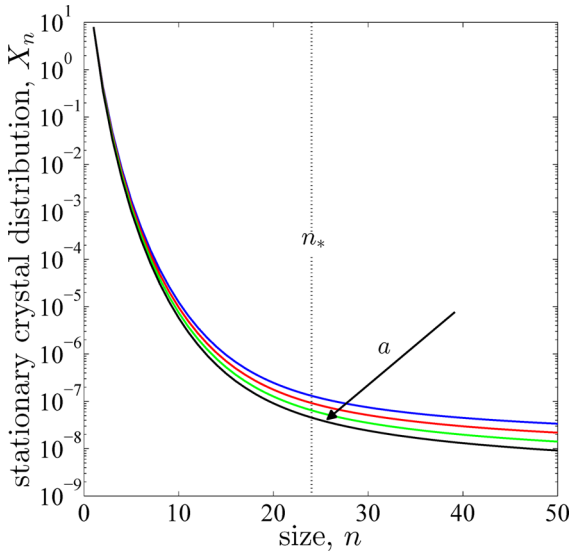

Figure 4. Unseeded simulations at constant supersaturation. Stationary crystal size distributions obtained at small crystal sizes for different values of the exponent a. The values of a are 1/3, 4/9, 5/9, and 2/3. The simulations have been performed with a supersaturation $S = 8$ and a dimensionless capillary length $\alpha = 6$. The critical size, n_*, is indicated by the dashed line.

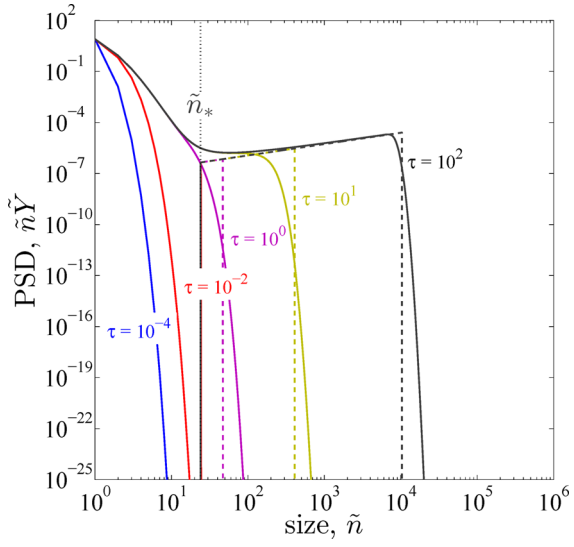

Figure 5. Unseeded simulations at constant supersaturation. Comparison of the results of the classical PBE (dashed lines) to the results of the model based on the kinetic rate equation (solid lines). The different colors represent the PSD at different times. It should be noted that the PSDs for the classical PBE model partially overlap, so only the vertical/near-vertical "front" is clearly visible for all different times for both models. The data represented in this figure stem from a simulation with a supersaturation $S = 8$ and a dimensionless capillary length $\alpha = 6$.

solution. Finally, simulations of unseeded processes at varying supersaturation are presented. In these last simulations, crystals are first nucleated, then grown, and finally subjected to Ostwald ripening. As explained in the introductory part of this work, such simulations cannot be carried out in a continuous fashion using a single, classical PBE model but are unique of the KRE model.

In all the simulations, the kinetic rate equation model in its dimensionless form is solved numerically using the multiscale approach presented in section 2.2. While the ordinary differential equations in the discrete part of the model can easily be solved by standard integration techniques (in our case, we use MATLAB's ode15s,[50,51] a multistep solver tailored explicitly to solving stiff problems), the Fokker–Planck equation in the continuous part of the model is solved using a discretization scheme first proposed by Chang and Cooper,[52] which has already been applied to model the nucleation and growth of nanocrystals.[28,53] The discretized equations are then again solved with ode15s. We report the detailed procedure in the Supporting Information (Appendix C). Solutions of the classical PBE model in its dimensionless form are reported for simulations at constant supersaturation. In these cases, the solution can be calculated analytically using the method of characteristics.[54]

3.1. Simulations at Constant Supersaturation.

3.1.1. Simulations of Unseeded Processes: Nucleation. Simulations of unseeded processes at constant supersaturation are ideally suited to investigate nucleation since many transient phenomena, caused by a varying supersaturation, are eliminated. Keeping supersaturation constant therefore allows the investigation of a limiting case and is useful particularly from a conceptual point of view. An example of the simulation of such a case is shown in Figure 2 where the solution of the KRE model is shown as a contour plot, that is, the contour lines indicate level sets of $\tilde{Y}(\tau, \tilde{n})$. Note that the color scale used in this and the following contour plots is logarithmic and the same for all figures. Analyzing the evolution of the PSD shown in this plot, one sees that, in the KRE model, supercritical crystals appear only after some delay. This behavior is different from the classical PBE model, where constant supersaturation implies an immediate, linear increase in the number of crystals over time. In the KRE model, the instantaneous, dimensionless nucleation rate, ϕ, can be calculated from the time derivative of the number of supercritical crystals

$$\phi = \frac{\mathrm{d}}{\mathrm{d}\tau}\left(\sum_{i=\lceil \tilde{n}_* \rceil}^{N} Y_n + \int_{\max\{\tilde{n}_*, N+1\}}^{\infty} \tilde{Y}\, \mathrm{d}\tilde{n}\right) \tag{19}$$

As previously emphasized, in the KRE model, nucleation appears naturally from the interplay of attachment and detachment rates

dx.doi.org/10.1021/cg4010714 | Cryst. Growth Des. 2013, 13, 4890–4905

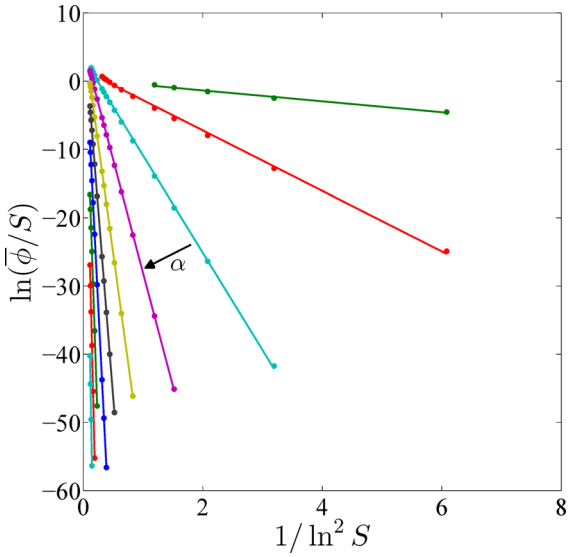

Figure 6. Unseeded simulations at constant supersaturation. Linearization of the stationary nucleation rates obtained with the KRE model. The symbols represent the simulated values while the lines represent the linear regressions on these sets of data points. For a list of simulations shown in this figure, refer to Table 1

without the need of an additional kinetic expression or parameters. In contrast, in the PBE model, a rate expression specific to nucleation (eq 4) is required, and the two additional model parameters K_1 and K_2 have to be assigned. The evolution of the number of supercritical crystals for the simulation illustrated in Figure 2 is shown in Figure 3, where the nucleation rate is shown to approach a constant value for the KRE model after an initial "lag time". Since the instantaneous dimensionless nucleation rate, $\phi(\tau)$, approaches the stationary value of the nucleation rate, $\bar{\phi}$, rather slowly, we define the lag time, τ_{lag}, as the time when the relative difference of the instantaneous and stationary dimensionless nucleation rate becomes smaller than a threshold:

$$\frac{\phi(\tau_{lag}) - \bar{\phi}}{\bar{\phi}} \leq \epsilon_{threshold} \tag{20}$$

Table 1. Overview of Unseeded Simulations at Constant Supersaturation

ID	α	S range
CU1a-e	1	1.5−2.5
CU2a-l	2	1.5−6
CU3a-p	3	1.75−16
CU4a-p	4	2.25−20
CU5a-n	5	3−20
CU6a-l	6	4−20
CU7a-j	7	5−20
CU8a-g	8	8−20
CU9a-f	9	10−20
CU10a-d	10	14−20

where the threshold was selected to be $\epsilon_{threshold} = 10^{-4}$. In the simulations reported in this work (cf. Table 1), we observed a maximal dimensionless lag time $\tau_{lag} \approx 10^3$. The values of the stationary dimensionless nucleation rate can be determined either by evaluating ϕ at large times ($\tau > 10^6$) or by calculating the flux between neighboring points in the discrete distribution under steady-state conditions

$$\bar{\phi} = \eta_n S X_n - \xi_{n+1} X_{n+1} \tag{21}$$

where X_n indicates the (dimensionless) steady-state distribution, which can be approximated from Y_n at large τ, and η_n and ξ_{n+1} are dimensionless attachment and detachment rate constants (see Appendix B in the Supporting Information). It is noteworthy that the shape of the stationary crystal size distribution depends on the value of a in the dimensionless attachment and detachment rate constants. To illustrate this, simulations for a values of 1/3, 4/9, 5/9, and 2/3 were performed, whose stationary crystal size distributions are reported in Figure 4. The change in the stationary distribution is counterbalanced by the change in the dimensionless attachment and detachment rates, $\eta_n S$ and ξ_n, so that the values obtained for $\bar{\phi}$ are the same, regardless of the value of a.

With the stationary nucleation rate determined from the above analysis, the KRE model output can be compared with

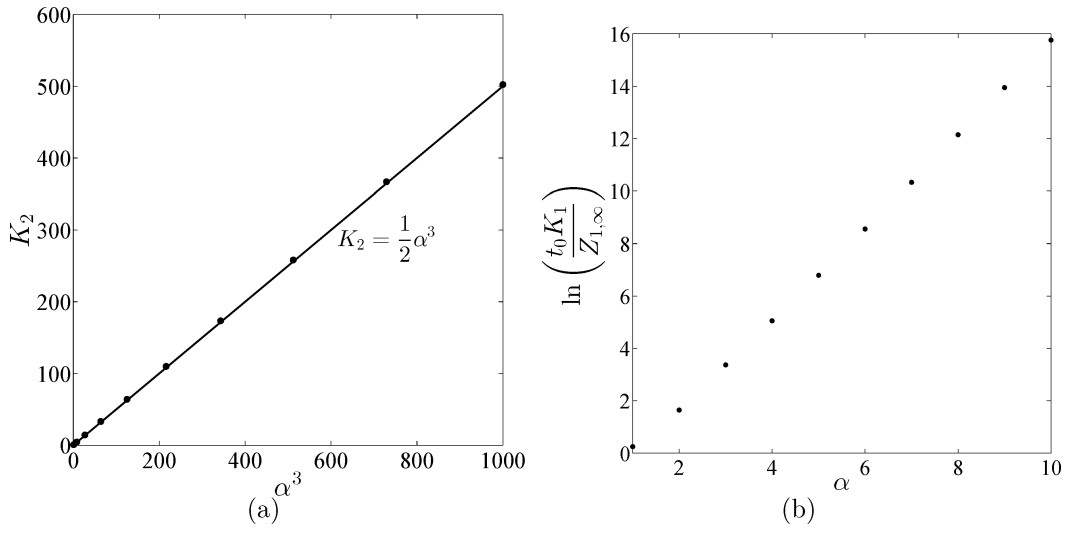

Figure 7. Unseeded simulations at constant supersaturation: (a) dependency of K_2 on α^3, (b) dependency of $\ln(t_0 K_1/Z_{1,\infty})$ on α. The values of K_1 and K_2 have been obtained from the linearizations of the nucleation rates reported in Figure 6, which in turn have been determined from the simulations reported in Table 1.

dx.doi.org/10.1021/cg4010714 | Cryst. Growth Des. 2013, 13, 4890−4905

Table 2. Overview of Seeded Simulations at Constant Supersaturation

ID	α	$\bar{n}_0$	σ_0	S	ψ
CS1a-d	1	1×10^7	5×10^7	{1.1, 1.4, 1.7, 2}	0.05
CS2a-d	5	1×10^7	5×10^5	{1.1, 1.4, 1.7, 2}	0.05
CS3a-d	10	1×10^7	5×10^5	{1.1, 1.4, 1.7, 2}	0.05
CS4a-d	1	1×10^{10}	5×10^8	{1.1, 1.4, 1.7, 2}	0.05
CS5a-d	5	1×10^{10}	5×10^8	{1.1, 1.4, 1.7, 2}	0.05
CS6a-d	10	1×10^{10}	5×10^8	{1.1, 1.4, 1.7, 2}	0.05
CS7a-d	1	1×10^{13}	5×10^{11}	{1.1, 1.4, 1.7, 2}	0.05
CS8a-d	5	1×10^{13}	5×10^{11}	{1.1, 1.4, 1.7, 2}	0.05
CS9a-d	10	1×10^{13}	5×10^{11}	{1.1, 1.4, 1.7, 2}	0.05

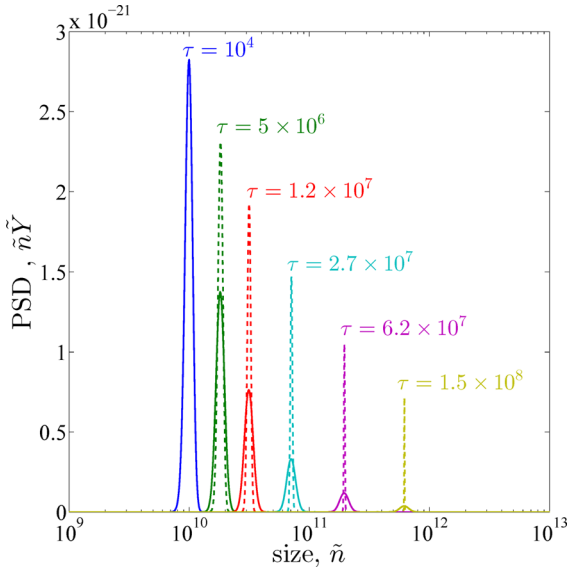

Figure 8. Seeded simulations at constant supersaturation. Particle size distribution at selected time points for the KRE model (solid lines) and the PBE model (dashed lines).

the (analytical) solution of the PBE model with an identical nucleation rate. The result is given in Figure 5, where the PSD is shown at different times during the process. While the solutions of the two models show similarities, several differences can be identified: first, as already outlined, the KRE model describes both sub- and supercritical crystals, while

Table 3. Overview of Seeded Simulations at Varying Supersaturation

ID	α	S_0	$\bar{n}_0$	σ_0	ψ
VS1	5	1	1.5625×10^7	1×10^8	1.5
VS2	5	1	1.25×10^8	1×10^8	1.5
VS3	5	1	1×10^9	1×10^8	1.5
VS4	5	1	3.375×10^9	1×10^8	1.5
VS5	5	1	8×10^9	1×10^8	1.5
VS6	5	1	1.5625×10^{10}	1×10^8	1.5

the PBE model only accounts for supercritical crystals; second, the PSDs obtained from the KRE model have a "front" that is not as sharp as the ones obtained by the PBE model. Upon comparison of the PBE (eq 1) and the continuous version of the KRE (the Fokker–Planck equation, eq 10), it is clear that the second-order term in the Fokker–Planck equation causes the unsharp front. However, one should be aware that the Fokker–Planck equation is merely a consequence of the Taylor expansion applied to the discrete kinetic rate equation (eq 7) in order to arrive at a continuous equation. Hanggi et al.,[55] Shizgal and Barrett,[56] and Wu[57] provide an extensive overview of alternative ways to arrive at a continuous equation and discuss their accuracy (with respect to describing the discrete KRE). However, none of these alternatives is equivalent to the PBE, which is not surprising because the description of nucleation in the two models is quite different, that is, the direct formation of a crystal of critical size in the PBE vs the growth of sub- to supercritical crystals in the KRE. It is noteworthy that the unsharp fronts seen in the KRE model are *not* merely a result of numerical dispersion, which we have kept insignificant by using a discretization grid with geometrical spacing and a fine resolution (see Appendix C in the Supporting Information for details).

Overall, the solutions of the two models for the simulation presented in Figure 5 are remarkably similar despite the different assumptions made in their derivation. To analyze the dependence of the stationary nucleation rate on the supersaturation and the capillary length, the simulations listed in Table 1 have been performed ($a = 1/3$ for all simulations in this table and all subsequently presented simulations).

The stationary nucleation rates from these simulations, together with the classical nucleation rate equation, eq 18, can

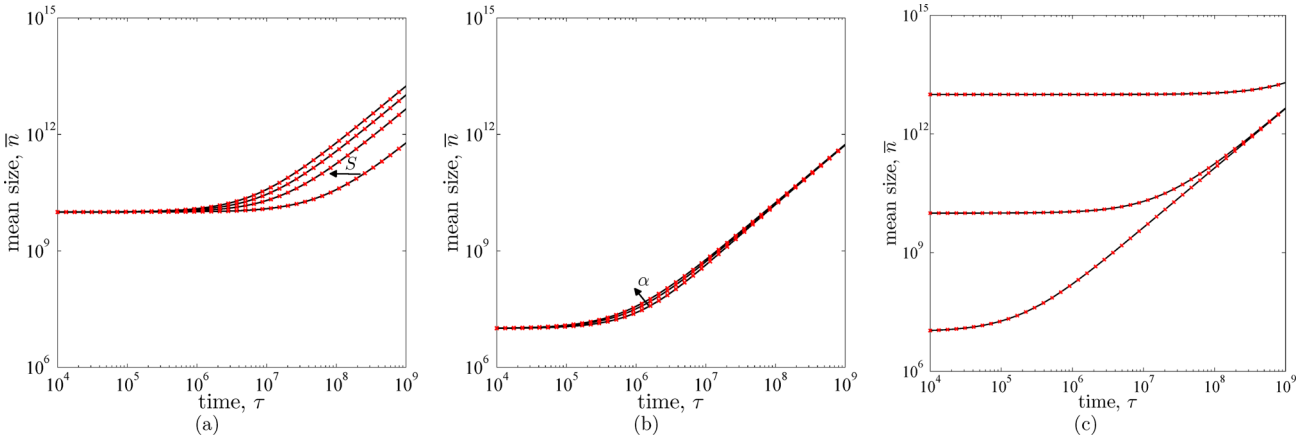

Figure 9. Seeded simulations at constant supersaturation. Effect of changing parameters on the evolution of the mean size, $\bar{n}$, in the PBE (×) and KRE (—) models: (a) effect of different levels of supersaturation (simulations CS5a-d in Table 2), (b) effect of the dimensionless capillary length α (simulations CS1a, CS2a and CS3a in Table 2), (c) effect of different initial particle sizes (simulations CS2c, CS5c and CS8c in Table 2).

dx.doi.org/10.1021/cg4010714 | Cryst. Growth Des. 2013, 13, 4890–4905

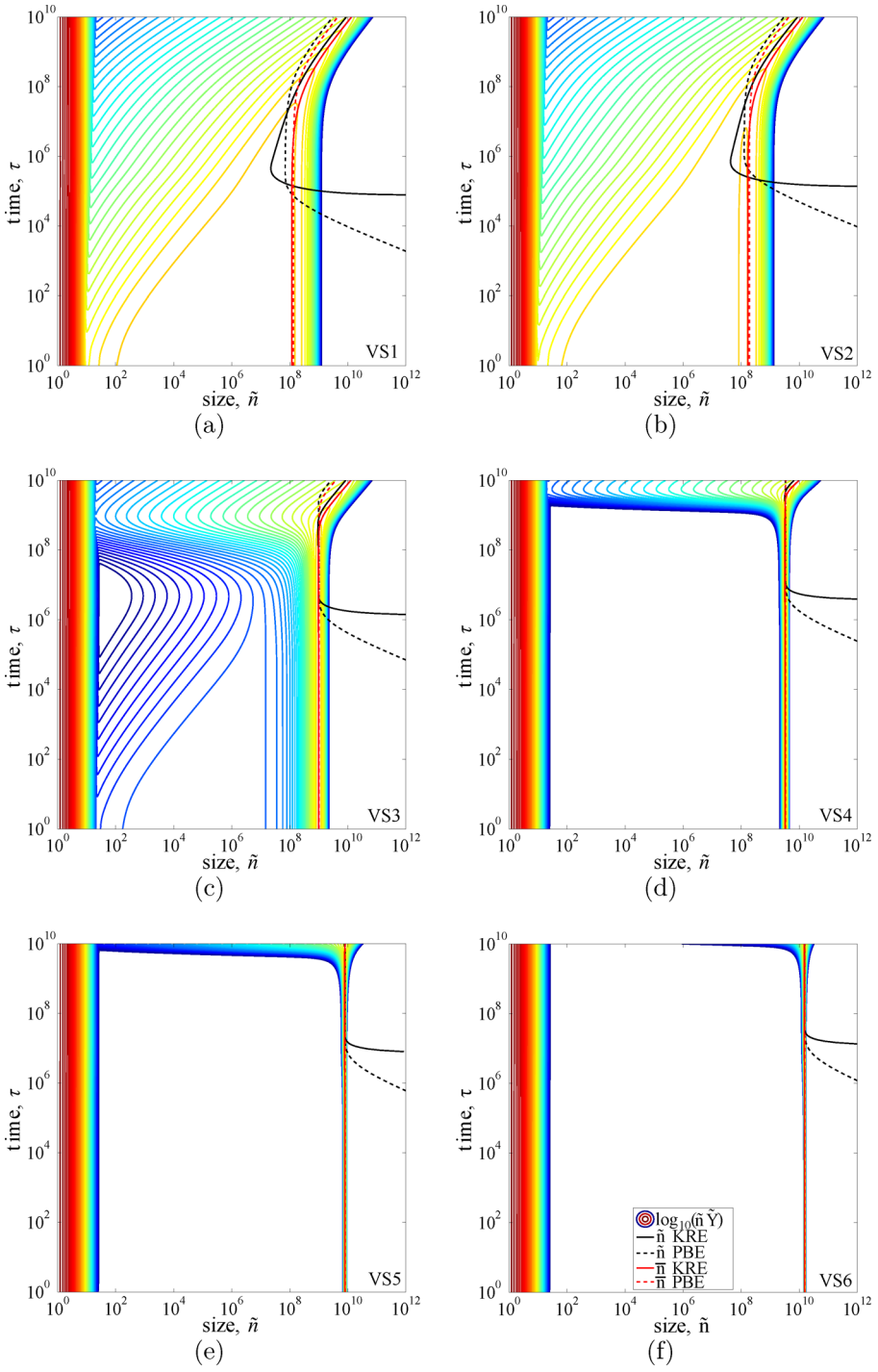

Figure 10. Seeded simulations at varying supersaturation. Complete evolution of the volume-weighted particle size distributions (contour plots), critical size (black lines), and mean particle size (red lines). Results from the KRE model are shown as solid lines, and results from the PBE model are shown as dashed lines. The color scale for the contour lines is the same as used in Figure 2. The mean size of the seeded particles increases from VS1 to VS6, that is, from panel a to f. See Table 3 for details of the parameters used in these simulations.

be used to find parameter pairs of K_1 and K_2 at given capillary lengths, as shown in Figure 6.

In Figure 7, $\ln(t_0K_1/Z_{1,\infty})$ and K_2 are plotted as functions of α and α^3, respectively. For the specific functional form of attachment and detachment rates chosen in this work (eqs 8 and 9), these plots show that there is a clear dependence of the ordinate values on α; that is, one can see in Figure 7a that our simulation data is consistent with the relationship for K_2 derived earlier, that is, $K_2 = \alpha^3/2$. Similarly, in Figure 7b, one sees that the dependence of $\ln(t_0K_1/Z_{1,\infty})$ on α can be described by an affine function. Explicitly, this function is

$$\ln(t_0K_1/Z_{1,\infty}) = 1.74\alpha - 1.79 \tag{22}$$

The coefficient of determination by eq 22 is $R^2 = 0.9993$. This means that as soon as the value of α is known and the attachment and detachment rates are defined, the corresponding values of K_1 and K_2 follow. This indicates that, under the given conditions, K_1 and K_2 introduced in classical nucleation

dx.doi.org/10.1021/cg4010714 | Cryst. Growth Des. 2013, 13, 4890−4905

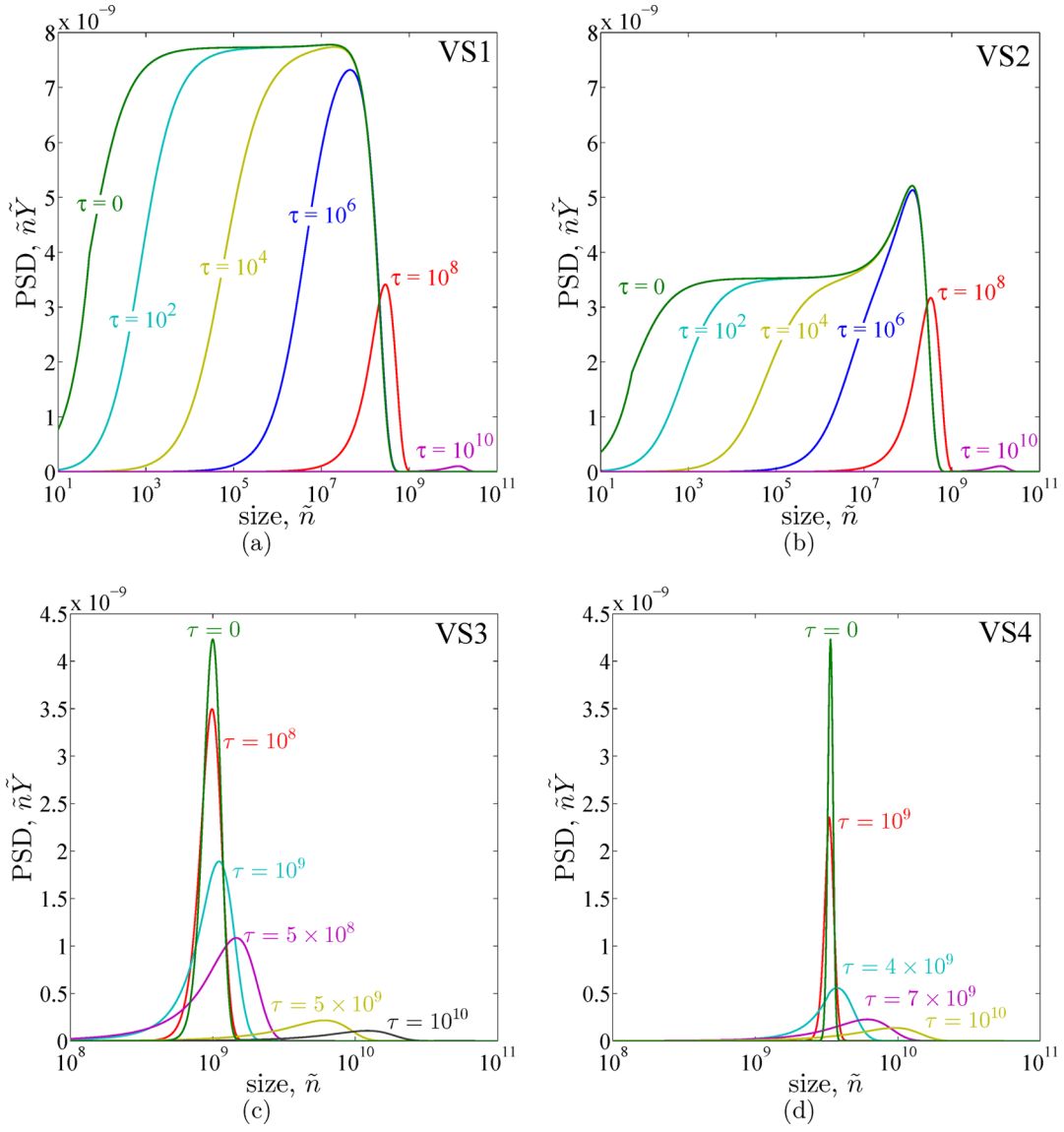

Figure 11. Seeded simulations at varying supersaturation. PSDs at selected times for simulations VS1−4. The mean size of the seeded particles increases from VS1 to VS4, that is, from panel a to d. See Table 3 for details of the parameters used in these simulations.

theory are not independent parameters as normally assumed in classical population balance equation models.

Testing the above postulated dependence of $\ln(t_0K_1/Z_{1,\infty})$ on α against experimental observations would be an attractive and necessary task. However, such a validation is made practically impossible by the following two considerations about our model assumptions as compared with the operating conditions of laboratory experiments: (1) In solution crystallization, the supersaturation is often generated either by cooling or by antisolvent addition. Both techniques affect the surface tension and therefore the dimensionless parameter α in an *a priori* unknown way, thus making the interpretation of the nucleation rates reported in the literature in the context of our model exceedingly hard. (2) The crystal growth rate is frequently measured with large crystals that are orders of magnitude larger than critical nuclei. These measured growth rates are unlikely to apply to very small crystals.

To the best of our knowledge, there is no data set for a single compound crystallized from solution that is not affected by these considerations, so the validation of our simulation results against experimental data cannot (yet) be carried out. Therefore, the above-mentioned dependence of $\ln(t_0K_1/Z_{1,\infty})$ on α simply remains a property that we observed by performing thorough and comprehensive simulations with the KRE model.

3.1.2. Simulations of Seeded Processes: Crystal Growth. We now focus our attention on the description of crystal growth at constant supersaturation in the PBE and KRE model. To this end, a series of seeded simulations is performed where the seed distributions considered are normal distributions with mean at $\bar{n}_0$ and standard deviation of σ_0, as reported in Table 2. To correctly focus on the mechanism of growth only, nucleation is artificially deactivated in both the PBE and KRE model. In the case of the PBE model, this is achieved by setting $\bar{\phi} = 0$, while in the case of the KRE model, nucleation is removed by setting the flux from $n = 1$ to $n = 2$ to zero. The amount of seed particles added to each simulation is defined by the initial holdup ratio ψ, defined as the ratio between the number of molecules initially present in the solid phase to the number of molecules initially in the liquid phase:

$$\psi = \frac{\mu_1(\tau = 0)}{S_0} \tag{23}$$

dx.doi.org/10.1021/cg4010714 | *Cryst. Growth Des.* 2013, 13, 4890−4905

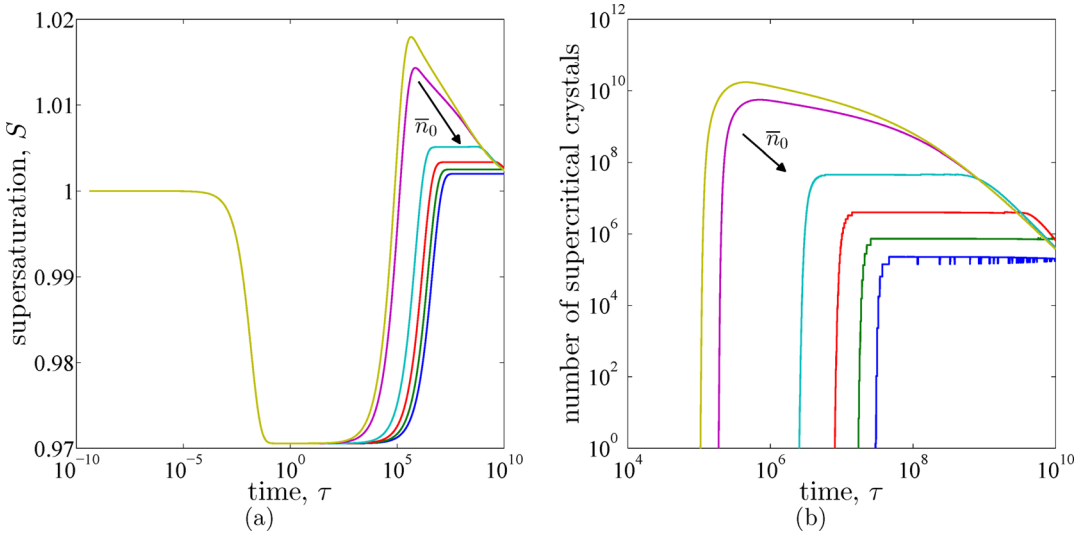

Figure 12. Seeded simulations at varying supersaturation. Integral properties of the simulations: (a) evolution of supersaturation, (b) evolution of number of supercritical crystals.

where S_0 is the initial supersaturation and $\mu_1(\tau = 0)$ is the first moment of the initial distribution. The dimensionless moments are thereby given by

$$\mu_j = \int_0^\infty \tilde{n}^j \tilde{Y}\, \mathrm{d}\tilde{n} \tag{24}$$

for the PBE model, and as

$$\mu_j = \sum_{n=2}^{N} n^j Y_n + \int_{N+1}^\infty \tilde{n}^j \tilde{Y}\, \mathrm{d}\tilde{n} \tag{25}$$

for the hybrid kinetic rate equation model.

Solving the PBE and KRE model for the cases reported in Table 2, one obtains the evolution of the PSD over time. An example of such an evolution for both models (simulation CS5c in Table 2) is shown in Figure 8, where the volume-weighted PSD is plotted for both models at specific values of the dimensionless time. One immediately sees that the PSD in the two models evolves similarly, that is, the mode of the distribution behaves the same in both models. However, the width behaves differently. In the case of the KRE model, we clearly see a broadening of the PSD over time, while the width of the PSD decreases in the PBE model, as one would expect using the growth rate defined in eq 13. Similar to the nucleation simulation presented in Figure 5, where the "front" of the PSD was observed to be less sharp for the KRE model than for the PBE model, the widening of the PSD is again a direct consequence of the second-order term in the Fokker–Planck equation.

In order to quantify the effects of varying α, S, and seed distribution, we define the volume-weighted mean size of the particles in the PSD as

$$\overline{n} = \frac{\mu_2}{\mu_1} \tag{26}$$

The evolution of the mean size for exemplary simulations for both the KRE and PBE model is shown in Figure 9. Focusing on the PBE model (black lines), the evolution of the mean size follows the dependency of the growth rate (eqs 3, and 13) on the varied parameters, that is, an earlier increase of the mean size is observed at higher supersaturations (Figure 9a), lower α values (Figure 9b), and smaller initial particle sizes (Figure 9c). One can see from all three subfigures that the mean size evolves identically in both models for all sets of parameters, so that one can conclude that the KRE models and the PBE models agree well in their description of crystal growth.

3.2. Simulations at Varying Supersaturation. *3.2.1. Simulations of Seeded Processes: Ostwald Ripening.* Let us now shift our attention from nucleation and growth to Ostwald ripening in this section. To investigate this mechanism, it is necessary to let the supersaturation vary over time; that is, we relax the constant supersaturation assumption of the previous section. Ostwald ripening is a phenomenon that has been investigated using a plethora of models. Iggland and Mazzotti[26] recently published an overview of these models and used a full PBE model to simulate and analyze Ostwald ripening. In this work, we compare simulations using the KRE model to simulations with the PBE model, while keeping the same parameters in both models. To this end, we report a series of simulations starting from a saturated solution that contains different-sized particles, for which the values of the relevant parameters are reported in Table 3.

The complete evolution of the volume-weighted PSD calculated using the KRE model for increasingly large seed distributions (see Table 3) is reported in the form of contour plots in Figure 10 (note that the seeds are normally distributed in $\tilde{Y}$ while $\tilde{n}\tilde{Y}$ is plotted). In the same plot, we compare the volume-weighted mean particle size (red lines) and critical size (black lines) obtained using the two models. For all simulations, the critical size lies initially outside the investigated size region (since we start from a saturated solution, the critical size is infinitely large); it is only after a certain time period that it enters the observed size region. This decrease in critical size is due to a rise in supersaturation, which in turn is caused by a net dissolution of particles. Because larger particles take considerably longer to fully dissolve, this delay is an increasing function of seed size, which is in accordance with experimental observations where Ostwald ripening is effectively negligible for sufficiently large particles.

Eventually, the critical size is small enough to make a sizable fraction of the particles become supercritical. This has an impact on the distribution because now the dissolution of

dx.doi.org/10.1021/cg4010714 | Cryst. Growth Des. 2013, 13, 4890−4905

crystals is additionally enhanced by the consumption of solute by the largest particles. This system of simultaneous dissolution and growth may remain in a fragile balance for awhile, as indicated by the constant critical size in some plots, particularly for larger seed crystals. Ultimately, however, the average size starts to increase and a net decrease of supersaturation can be observed with the critical size now trailing the mean size of the particles, both fingerprints of Ostwald ripening.

Focusing on the contour lines given by the solution of the KRE model, it can be seen that, immediately at the beginning, small sized clusters are formed in all simulations. Also, the rearrangement of the PSD due to dissolution of subcritical particles is evident.

The effect of this dissolution on the PSD in different simulations is also visible in Figure 11, where volume-weighted PSDs at specific points in time are reported. Since almost no change in the PSD can be observed for the large seed particles (simulations VS5 and VS6), these simulations are omitted from the analysis. Again, the outlined behavior can be observed: the change in the PSD starts by dissolving particles while the mode of the PSD remains quasi-stationary. When sufficient crystals are dissolved, the remaining particles begin to increase in size, which can be seen by the modes of the PSDs shifting to larger sizes.

We additionally report two important integral quantities obtained from the simulations in Figure 12: the evolution of supersaturation and the evolution of the number of supercritical particles. The evolution of supersaturation, cf. Figure 12a, exhibits a peculiar behavior because it indicates that the initially saturated solution becomes undersaturated at early times of the simulation. This effect is considered purely kinetic: since the formation of unstable oligomers is kinetically favored in comparison to single solute molecules and since we defined the supersaturation purely on the basis of the single solute molecules (Y_1), this causes the supersaturation to decrease. Hence, this mathematical artifact is unlikely to be observed in reality (i.e., experimentally). However, the evolution of the supersaturation at later stages is consistent with LSW theory, that is, the peak in supersaturation occurs slightly earlier and is higher for smaller seed particles than for larger ones. Focusing now on the evolution of the number of supercritical crystals (cf. Figure 12a) we notice that the number of supercritical particles initially increases, which is caused by the fact that the critical size is infinitely large at the beginning. It has to be stressed that this increase in the number of supercritical crystals is *not* associated with nucleation, as can be clearly seen from the evolution of the PSDs in Figures 10 and 11. However, we observe again a consistent behavior at later stages of the simulations, that is, the rate of disappearance of supercritical crystals becomes the same for all the simulations.

The outlined behavior is the same in the PBE model of Ostwald ripening,[26] and is also predicted by the LSW theory.[20,21] In the asymptotic growth stage, the change in the mean particle size (solid red line for the KRE model; dashed red line for the PBE model) and critical size (solid black line for the KRE model; dashed black line for the PBE model) is the same in both models. The behavior in the early stages of the simulation is slightly different, especially in the simulations with small seed particles. This difference is caused by the clusters, whose generation at the very beginning of the simulations interferes with the seed particles, thereby affecting the evolution of the system. Comparing the two models, one observes that the KRE model predicts a quantitatively comparable behavior to the PBE model, with differences caused by the presence of clusters.

3.2.2. Simulations of Unseeded Processes: Nucleation, Crystal Growth, and Ostwald Ripening. The real strength of the KRE model becomes apparent when unseeded simulations starting from a supersaturated solution are investigated. In these simulations, crystals nucleate and grow before they finally undergo Ostwald ripening. By variation of the key simulation parameters, that is, the initial supersaturation and the capillary length, it is demonstrated that the KRE not only can model the entirety of this process, but is indeed able to do so under a wide range of operating conditions. The parameters used in the simulations are reported in Table 4. This type of simulation cannot be performed using a classical PBE model, and hence no direct comparison is possible. However, we will interpret the results in two ways: by using the complete evolution of the PSDs and by introducing characteristic times that allow us to identify dominating mechanisms at a specific time during the simulations.

Table 4. Overview of Unseeded Simulations at Constant Supersaturation

ID	α	S_0 range
VU1a−n	3	1.5−10
VU2a−n	4	1.5−10
VU3a−n	5	1.5−10
VU4a−n	6	1.5−10
VU5a−n	7	1.5−10
VU6a−n	8	1.5−10

In a first step, we focus on a single simulation and use both approaches to explain the evolution of the PSD in detail. Later on in this section, a comparative assessment of a larger set of simulations will be presented. Let us therefore consider a simulation at α = 4 and an initial supersaturation S_0 = 4 for which the evolution of the volume-weighted PSD and the critical size is illustrated in Figure 13 in the form of a contour

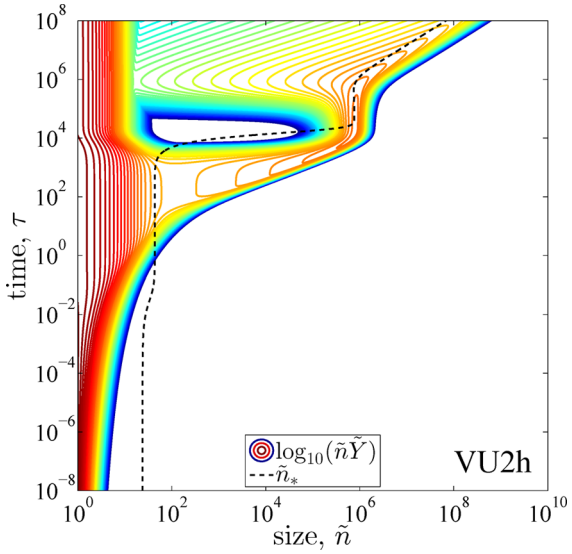

Figure 13. Unseeded simulations at varying supersaturation. Evolution of volume-weighted PSD for simulation VU2h with dimensionless capillary length α = 4 and initial supersaturation S_0 = 4. The dashed black line represents the critical size at the supersaturation present at that time. The color scale for the contour lines is the same as used in Figure 2.

dx.doi.org/10.1021/cg4010714 | Cryst. Growth Des. 2013, 13, 4890−4905

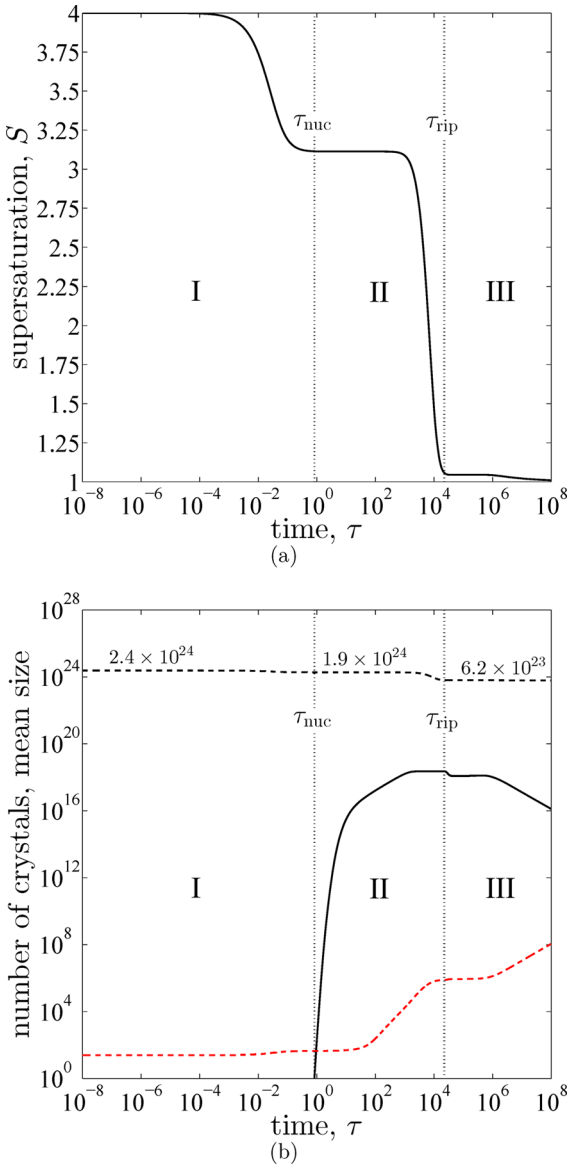

Figure 14. Unseeded simulations at varying supersaturation. Integral properties of simulation VU2h with dimensionless capillary length α = 4 and initial supersaturation S_0 = 4: (a) supersaturation over time, (b) number of supercritical crystals over time (solid line) and concentration of solute molecules, Z_1 (black dashed line) and mean size of supercritical crystals (red dashed line). The characteristic nucleation and ripening time, τ_{nuc} and τ_{rip}, are indicated with black dotted lines in both panels.

plot, while we report the evolution of the supersaturation and the number of supercritical crystals in Figure 14a,b, respectively. Note that in Figure 13, as before, contour lines in red represent the largest values of the PSD, whereas those in blue represent the lowest values, with the transition from red to blue given by the yellow and green hues, where the color scale is distributed logarithmically, so that it spans 25 orders of magnitude from 10^{-24} to 10; note also the logarithmic scales used for both time and particle size. In Figure 14b, the number of supercritical crystals is not smooth because of the discretized nature of our numerical solution to the kinetic rate equations. Finally, it should be noted that the number of solute molecules per suspension volume (i.e., Z_1) is massive, so the contour lines in the very small size range will always be shown in red color, even when the supersaturation has almost been depleted at the end of the process. To highlight this fact, we have reported Z_1 in a separate curve in Figure 14b and have explicitly written the number of molecules at the plateau values of the supersaturation (cf. Figure 14a) on top of this curve.

Analyzing the contour lines in Figure 13, we first see a "relaxation" process, that is, the rapid formation of subcritical clusters (on the left side of the critical size). The formation of these clusters consumes a small amount of supersaturation (cf. Figure 14a), but no supercritical crystals have been formed yet. With increasing time, the subcritical clusters grow and a small number of supercritical crystals are formed around τ = 1 (i.e., slightly after the first contour lines cross the critical size). We define the formation of the first supercritical crystal as the nucleation time, τ_{nuc}, which shall be one of our two characteristic process times. The nucleation time marks the boundary between the relaxation phase (marked as I in Figure 14) and the nucleation and crystal growth phase (marked with II in Figure 14). Directly following the formation of the first supercritical crystal, nucleation is the dominant process (from τ = 1 until $\tau \approx 10^3$) and many more nuclei are formed as can be seen in Figure 14b. However, the number of supercritical crystals reaches a plateau at $\tau \approx 10^3$, while the supersaturation is sharply decreasing from $\tau \approx 10^3$ to $\tau \approx 10^4$. This is due to crystal growth that consumes a large number of solute molecules in this phase. The growth process can also clearly be identified by the significant increase in the average size of the supercritical crystals that can either be seen from the contour lines of the distribution, cf. Figure 13, or in Figure 14b where the mean size of the supercritical crystals is reported directly. Note that the growth rate used in this work (eq 13) and the sharp decrease in supersaturation lead to a focusing of the size distribution that ends in a bimodal distribution consisting of subcritical clusters and supercritical crystals that are rather narrowly distributed. At the end of the crystal growth period, the supersaturation reaches another plateau and the number of supercritical crystals is at a maximum. We define this point, that is, where the number of supercritical crystals is maximal, as the ripening time, τ_{rip}, which signifies the end of the nucleation and crystal growth phase and the start of the process phase where Ostwald ripening becomes (potentially) important (marked with III in Figure 14). From this point onward, the evolution of the process follows the behavior of the simulations presented in section 3.2.1: a stationary period where the dissolution of the smaller particles in the distribution counterbalances the growth of the larger particles is followed by a period in which the supersaturation decreases slowly while the critical size and mean particle size increases accordingly.

Widening our scope now onto a larger set of simulations with α = 4 and initial supersaturations S_0 = 1.5, 3, 5, and 10, cf. Figures 15 and 16, we can investigate how the different process phases are affected by the change in initial supersaturation. Considering Figure 15, we see that the onset of nucleation is observed at earlier times for increasing initial supersaturations, and thus the relaxation phase is shorter, which is consistent with experimental observations where measured induction times are shorter at higher initial supersaturations. Note that the simulation at the lowest initial supersaturation (depicted in Figure 15a) remains in a metastable state and the formation of supercritical crystals is not observed within the time frame of the simulation. Comparing panels b and c to Figure 13, one can see that precipitated particles at the end of the nucleation and growth phase are smaller for higher initial supersaturations and

dx.doi.org/10.1021/cg4010714 | Cryst. Growth Des. 2013, 13, 4890−4905

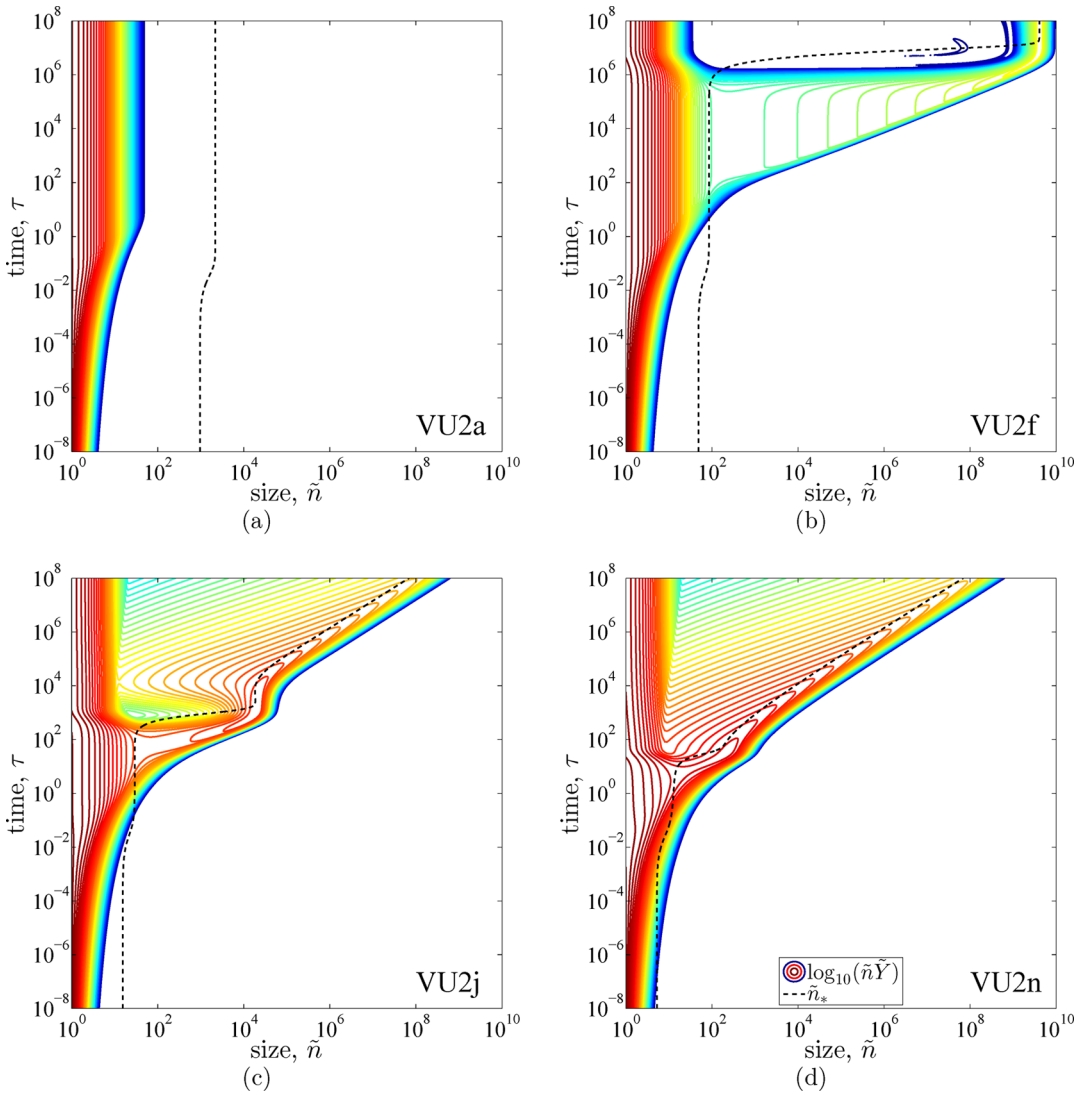

Figure 15. Unseeded simulations at varying supersaturation. Evolution of volume-weighted PSDs. The dashed black line represents the critical size at the supersaturation present at that time. The initial supersaturation is different in each panel, while the dimensionless capillary length is always $\alpha = 4$: (a) simulation VU2a, $S_0 = 1.5$, (b) simulation VU2f, $S_0 = 3$, (c) simulation VU2j, $S_0 = 5$, (d) simulation VU2n, $S_0 = 10$.

that the ripening phase consequently starts earlier. Note that for the highest initial supersaturation, $S_0 = 10$ (Figure 15d), a clear identification of the different phases is difficult because the transitions between the phases are blurry and nucleation, crystal growth, and Ostwald ripening are concomitant during the transitions.

Focusing our attention on the supersaturation profiles reported in Figure 16a and the number of supercritical crystals reported in Figure 16b for the simulations where significant Ostwald ripening can be observed ($S_0 = 4$, 5, and 10, that is, the purple, turquoise, and red lines), we can confirm our earlier observation (section 3.2.1) that no matter the distribution at the start of the ripening phase (i.e., the particles precipitated in the nucleation and growth phase) a consistent behavior at later stages of the simulations is observed, that is, the rate of disappearance of supercritical crystals and the decrease in supersaturation become the same for all the simulations.

The dependence of the two characteristic times, τ_{nuc} and τ_{rip}, on the initial supersaturation and the capillary length can be shown more comprehensively using the whole simulation set in Table 4. Hence, the characteristic times are plotted in Figure 17. It should be noted that the characteristic times were only determined for simulations where the different phases of the crystallization process could be clearly separated, so the number of simulations in Table 4 is larger than the number of data points in Figure 17. One can see that both characteristic times are shorter for shorter capillary lengths and for higher intitial supersaturations. This behavior is not surprising since τ_{nuc} is directly dependent on the nucleation rate, which in turn is higher for lower capillary lengths and higher initial supersaturations. The ripening time, τ_{rip}, decreases for higher initial supersaturations and lower capillary lengths because smaller crystals are obtained after the process phases of relaxation, nucleation, and crystal growth, as shown in Figure 15.

This information on characteristic times, which is only accessible via the complete description of the KRE model, could in principle be used to choose the operating conditions for a process in which both nucleation and ripening occur. For example, in a precipitation process, it might be desirable to delay Ostwald ripening as long as possible after particle formation, that is, prolonging the stationary phase prior to the onset of Ostwald ripening. A (qualitative) understanding of

dx.doi.org/10.1021/cg4010714 | *Cryst. Growth Des.* 2013, 13, 4890−4905

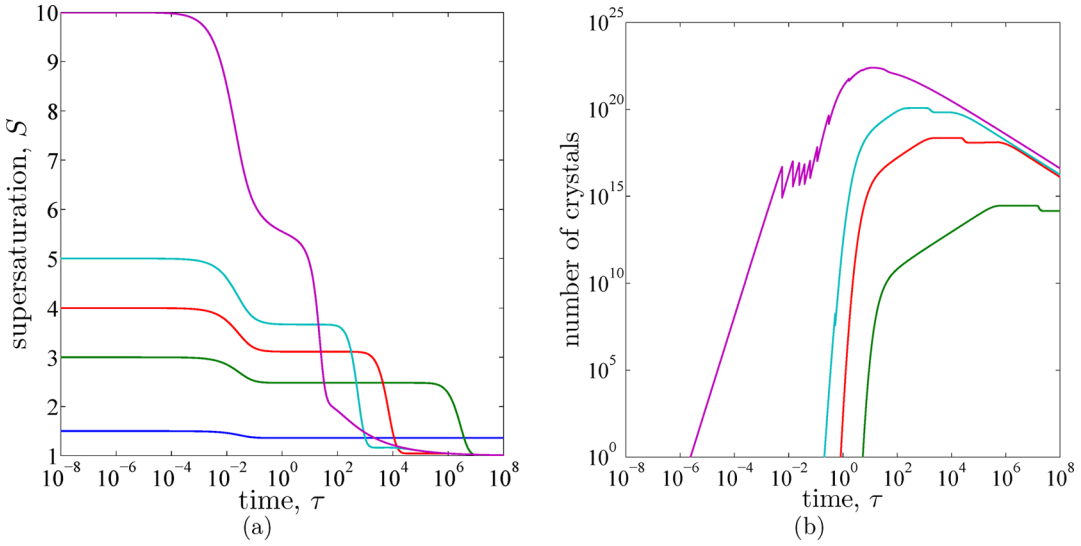

Figure 16. Unseeded simulations at varying supersaturation. Integral properties of simulations VU2a, VU2f, VU2h, VU2j, and VU2n with dimensionless capillary length $\alpha = 4$ and different initial supersaturations: (a) supersaturation over time, (b) number of supercritical crystals over time. The same line color corresponds to the same simulation in both panels. Note that in simulation VU2a ($S_0 = 1.5$, blue line in panel a) no supercritical crystals are formed, such that no line for this simulation is visible in panel b.

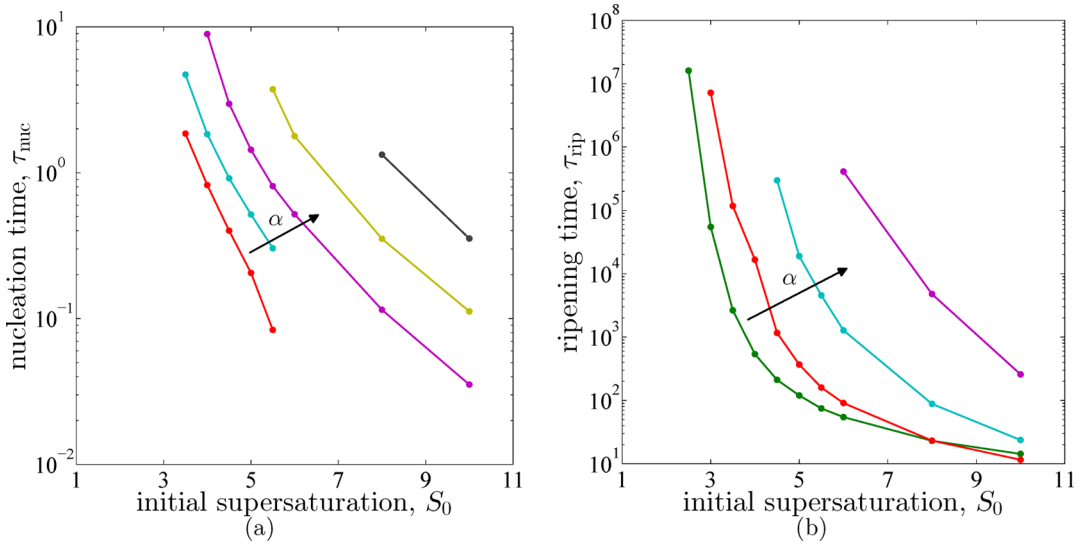

Figure 17. Unseeded simulations at varying supersaturation. Characteristic times: (a) nucleation times, τ_{nuc}; (b) ripening times, τ_{rip}. Note that the same color has been used to represent the same dimensionless capillary length, α, in the two panels.

how to accomplish this can be gained by considering the ratio of the two characteristic times, that is, τ_{rip}/τ_{nuc}. One would then wish to operate the precipitation process at a large value of this ratio by choosing appropriate operating conditions, S_0 and α. Clearly, this is a simplification of the real problem, where both physical limitations and constraints on the target PSD would need to be taken into account as well; however, the presented analysis defines a simple number that can be used to circumvent an otherwise elusive problem.

4. CONCLUDING REMARKS

In this work, two different ways of describing crystallization processes have been presented. The classical PBE model is based mainly on thermodynamic considerations, while the second type of model is based on the KRE. We have shown that the KRE model allows the simulation of all stages of a crystallization process in a single description by virtue of being self-consistent and avoiding some of the strong assumptions that are used in PBE models.

The kinetic KRE was solved using a hybrid approach with a discrete and a continuous part, where the latter is described by a Fokker−Planck equation. The resulting model yields a good trade off between accuracy and efficiency. However, the solution of this model is still more costly than solving a PBE of similar accuracy, which can be seen as a disadvantage of the KRE model.

By writing both the PBE and KRE models in dimensionless form, we have identified key parameters that influence the evolution of the particle size distribution. These parameters, initial supersaturation, initial particle size distribution, and capillary length, were subsequently varied in a parameter analysis. In order to compare the PBE and KRE models, different mechanisms present in a crystallization process (nucleation, crystal growth, and Ostwald ripening) were decoupled from each other by carefully

dx.doi.org/10.1021/cg4010714 | Cryst. Growth Des. 2013, 13, 4890−4905

choosing appropriate simulation conditions. We have confirmed for every mechanism separately that the KRE and PBE model deliver similar descriptions of the process and that the dependence of the two models on the key parameters given above is consistent. Nevertheless, the KRE model in general allows obtaining deeper insight into the behavior of both sub- and supercritical crystals.

A careful analysis of the results of simulations dedicated to investigate nucleation allowed us to align the parameters of the KRE and PBE models. The KRE model depends on only four parameters, namely, the nominal solubility $Z_{1,\infty} = c_\infty N_A$, the attachment rate constant, k, the constant exponent a in the attachment and detachment rates, and the constant α, related to the capillary length. For the PBE model, two additional (supposedly) independent parameters are typically introduced: K_1 and K_2. However, our analysis shows that K_1 and K_2 can in fact be expressed as functions of the remaining parameters, indicating that the degrees of freedom in the KRE and PBE models are the same.

We then proceeded to use the KRE model for simulations covering the whole crystallization process. For these simulations, it was thus possible to define characteristic times for the onset of nucleation and Ostwald ripening, so that the mechanism that is dominating during each phase of the crystallization process can be identified.

While the classical population balance equation approach is an irreplaceable tool for a wide variety of processes, we think that the unifying description of the KRE model that has been presented in this paper has conceptual and practical merits for certain applications. From a conceptual point of view, we consider the mechanisms of nucleation, crystal growth, and Ostwald ripening as different aspects of the same fundamental driving force (the difference in chemical potential) since they all involve the transfer of solute molecules from a disordered, liquid phase to an ordered crystalline phase. Consequently, the mechanisms should also be described in a consistent fashion. It is our strong belief that such a unifying, continuous description of these mechanisms, without artificially decoupling them, can be achieved by implementing and solving the KRE model.

From a practical perspective, the way the KRE model has been formulated allows for the accurate description of crystals below the critical size also during process stages where nucleation is present (or even dominating). In the light of recent studies that have shown that agglomeration of subcritical crystals might be an important aspect in nucleation,[47] the possibility to model these effects for the subcritical crystals is an important feature. Although not investigated in this work, such a mechanism could be implemented in a model based on the kinetic rate equations, while an implementation in a classical PBE model that describes nucleation to occur directly at the critical size would only be reflected in a correction of the nucleation rate (i.e., it would be increased), which is an unsatisfying oversimplification of the underlying physics. Finally, we have presented a possible pathway for how KRE simulations can yield an enhanced understanding regarding the choice of operating conditions for a particular process type.

■ ASSOCIATED CONTENT

Supporting Information

Derivation of size-dependent solubility and critical size, dimensionless versions of key equations in the PBE and KRE model, numerical solution scheme of the Fokker–Planck equation, and additional simulations of unseeded processes at varying supersaturation. This material is available free of charge via the Internet at http://pubs.acs.org/.

■ AUTHOR INFORMATION

Corresponding Author

*E-mail: marco.mazzotti@ipe.mavt.ethz.ch. Phone: +41 44 632 2456. Fax: +41 44 632 1141.

Present Address

§F.S.H.: Transport and Mobility Laboratory, EPF Lausanne.

Notes

The authors declare no competing financial interest.

■ NOTATION

a	exponent in the crystal growth rate regarding $\tilde{n}$ dependence [−]
A_n	crystal consisting of n molecules [−]
b	exponent in the crystal growth rate regarding concentration dependence [−]
c	solution concentration [mol m^{-3}]
c_∞	bulk solubility [mol m^{-3}]
$c_*(n)$	solubility of a crystal containing n molecules [mol m^{-3}]
$f(\tilde{n}, t)$	number-based particle size distribution [m^{-3}]
$g(\tilde{n})$	rate constant for attachment of a single molecule from a crysal of size n [m^3 s^{-1}]
$g(n, j)$	rate constant for attachment between crystals of size n and j [m^3 s^{-1}]
G	Gibbs free energy [J]
$h(\tilde{n})$	rate constant for the detachment of a single molecule from crystal of size n [s^{-1}]
$h(n, j)$	rate constant for the detachment of a crystal with size j from a crystal with size n [s^{-1}]
$H(\tilde{n})$	dispersion coefficient in the Fokker–Planck equation [s^{-1}]
J	nucleation rate [m^{-3} s^{-1}]
k	prefactor in the growth rate expression (eq 3) [m^{3b} s^{-1}]
K_1	prefactor in the nucleation rate expression (eq 4) [m^{-3} s^{-1}]
K_2	constant in the exponential part of the nucleation rate expression (eq 4) [−]
n	crystal size in number of molecules [−]
$\tilde{n}$	continuous crystal size in number of molecules [−]
$\tilde{n}_*$	critical size [−]
$\bar{n}$	mean particle size [−]
n_0	mean of seed distribution [−]
N	maximum particle size included in the discrete part of the multiscale model [−]
N_A	Avogadro constant [mol^{-1}]
R	ideal gas constant [J mol^{-1} K^{-1}]
S	supersaturation [−]
S_0	initial supersaturation [−]
t	time [s]
t_0	characteristic time [s]
T	temperature [K]
$v(\tilde{n})$	crystal growth rate [s^{-1}]
X_n	dimensionless concentration of crystals of size n under stationary conditions [−]
Y_n	dimensionless concentration of crystals of size n [−]
$\tilde{Y}(\tilde{n})$	dimensionless number density distribution in continuous form [−]
Z_n	concentration of crystals of size n [m^{-3}]
$Z_1^*(n)$	solubility of a crystal containing n molecules [m^{-3}]

$Z_{1,\infty}$ bulk solubility [m^{-3}]
$\tilde{Z}(\tilde{n})$ number density distribution of crystals in continuous form [m^{-3}]
α dimensionless capillary length [−]
δ Dirac delta function [−]
η_n dimensionless rate constant for the detachment of a single molecule from crystal of size n [−]
μ_j jth moment of $\tilde{Y}$ [−]
ξ_n dimensionless rate constant for the detachment of a single molecule from a crystal of size n [−]
ϕ instantaneous dimensionless nucleation rate [−]
$\bar{\phi}$ stationary dimensionless nucleation rate [−]
σ_0 standard deviation of seed distribution [−]
τ dimensionless time [−]
τ_{lag} lag time [−]
τ_{nuc} characteristic nucleation time [−]
τ_{rip} characteristic ripening time [−]
ψ initial hold up ratio [−]

REFERENCES

(1) Ostwald, W. *Z. Phys. Chem.* **1900**, *34*, 495−503.
(2) Voorhees, P. W. *J. Stat. Phys.* **1985**, *38*, 231−252.
(3) Randolph, A. D.; Larson, M. A. *Theory of Particulate Processes: Analysis and Techniques of Continuous Crystallization*; Academic Press: New York, 1971.
(4) Leblanc, S. E.; Fogler, H. S. *AIChE J.* **1987**, *33*, 54−63.
(5) Ramkrishna, D. *Population Balances: Theory and Applications to Particulate Systems in Engineering*; Academic Press: San Diego, CA, 2000.
(6) Kashchiev, D. *Nucleation*; Butterworth-Heinemann: Oxford, U.K., 2000.
(7) Mersmann, A., *Crystallization Technology Handbook*, 2nd ed.; Marcel Dekker: New York, 2001.
(8) Mullin, J. W., *Crystallization*, 4th ed.; Butterworth-Heinemann: Oxford, U.K., 2001.
(9) Volmer, M.; Weber, A. *Z. Phys. Chem.* **1926**, *119*, 277−301.
(10) Farkas, L. *Z. Phys. Chem.* **1927**, *125*, 236−242.
(11) Lindenberg, C.; Mazzotti, M. *J. Cryst. Growth* **2009**, *311*, 1178−1184.
(12) Lindenberg, C.; Mazzotti, M. *AIChE J.* **2011**, *57*, 942−950.
(13) Hulburt, H. M.; Katz, S. *Chem. Eng. Sci.* **1964**, *19*, 555−574.
(14) Tavare, N.; Garside, J. *Chem. Eng. Res. Des.* **1986**, *64*, 109−118.
(15) Randolph, A. D. *Ind. Eng. Chem. Fundam.* **1969**, *8*, 58−63.
(16) Kostoglou, M.; Dovas, S.; Karabelas, A. J. *Chem. Eng. Sci.* **1997**, *52*, 1285−1299.
(17) Zauner, R.; Jones, A. G. *Chem. Eng. Sci.* **2000**, *55*, 4219−4232.
(18) Kougoulos, E.; Jones, A. G.; Wood-Kaczmar, M. W. *J. Cryst. Growth* **2005**, *273*, 520−528.
(19) Lindenberg, C.; Schöll, J.; Vicum, L.; Mazzotti, M.; Brozio, J. *Cryst. Growth Des.* **2008**, *8*, 224−237.
(20) Lifshitz, I. M.; Slyozov, V. V. *J. Phys. Chem. Solids* **1961**, *19*, 35−50.
(21) Wagner, C. *Z. Elektrochem.* **1961**, *65*, 581−591.
(22) Tavare, N. S. *AIChE J.* **1987**, *33*, 152−156.
(23) Ståhl, M.; Åslund, B.; Rasmuson, Å. C. *Ind. Eng. Chem. Res.* **2004**, *43*, 6694−6702.
(24) Hoang, T. K. N.; Deriemaeker, L.; Finsy, R. *Langmuir* **2004**, *20*, 8966−8969.
(25) Liu, Y.; Kathan, K.; Saad, W.; Prud'homme, R. K. *Phys. Rev. Lett.* **2007**, *98*, No. 036102.
(26) Iggland, M.; Mazzotti, M. *Cryst. Growth Des.* **2012**, *12*, 1489−1500.
(27) Ozkan, G.; Ortoleva, P. *J. Chem. Phys.* **2000**, *112*, 10510−10525.
(28) Rempel, J. Y.; Bawendi, M. G.; Jensen, K. F. *J. Am. Chem. Soc.* **2009**, *131*, 4479−4489.
(29) Amal, Y.; Pinto, M. C. *Discrete Contin. Dyn. Syst. Ser. B* **2010**, *13*, 517−535.
(30) Madras, G.; McCoy, B. J. *Chem. Eng. Sci.* **2002**, *57*, 3809−3818.
(31) Noguera, C.; Fritz, B.; Clément, A.; Baronnet, A. *J. Cryst. Growth* **2006**, *297*, 180−186.
(32) Noguera, C.; Fritz, B.; Clément, A.; Baronnet, A. *J. Cryst. Growth* **2006**, *297*, 187−198.
(33) Uwaha, M.; Koyama, K. *J. Cryst. Growth* **2010**, *312*, 1046−1054.
(34) Dubrovskii, V. G.; Nazarenko, M. V. *J. Chem. Phys.* **2010**, *132*, No. 114507.
(35) Dubrovskii, V. G.; Nazarenko, M. V. *J. Chem. Phys.* **2010**, *132*, No. 114508.
(36) Dubrovskii, V. G.; Kazansky, M. A.; Nazarenko, M. V.; Adzhemyan, L. T. *J. Chem. Phys.* **2011**, *134*, No. 094507.
(37) Hounslow, M. J. *AIChE J.* **1990**, *36*, 106−116.
(38) Kumar, S.; Ramkrishna, D. *Chem. Eng. Sci.* **1997**, *52*, 4659−4679.
(39) Qamar, S.; Elsner, M. P.; Angelov, I. A.; Warnecke, G.; Seidel-Morgenstern, A. *Comput. Chem. Eng.* **2006**, *30*, 1119−1131.
(40) Rigopoulos, S. *Prog. Energy Combust. Sci.* **2010**, *36*, 412−443.
(41) Ono, T.; Kramer, H. J. M.; ter Horst, J. H.; Jansens, P. J. *Cryst. Growth Des.* **2004**, *4*, 1161−1167.
(42) Vetter, T.; Mazzotti, M.; Brozio, J. *Cryst. Growth Des.* **2011**, *11*, 3813−3821.
(43) Gherras, N.; Févotte, G. *AIChE J.* **2012**, *58*, 2650−2664.
(44) Stroock, D. W. *An Introduction to Markov Processes*; Springer: Berlin, Germany, 2005.
(45) Davey, R. J.; Garside, J. *From Molecules to Crystallizers: An Introduction to Crystallization*; Oxford University Press: Oxford, U.K., 2000.
(46) Kashchiev, D.; van Rosmalen, G. M. *Cryst. Res. Technol.* **2003**, *38*, 555−574.
(47) Yuk, J. M.; Park, J.; Ercius, P.; Kim, K.; Hellebusch, D. J.; Crommie, M. F.; Lee, J. Y.; Zettl, A.; Alivisatos, A. P. *Science* **2012**, *336*, 61−64.
(48) Kashchiev, D. *Cryst. Res. Technol.* **1984**, *19*, 1413−1423.
(49) Ohara, M.; Reid, R. C. *Modeling Crystal Growth Rates from Solution*; Prentice Hall: Upper Saddle River, NJ, 1973.
(50) Shampine, L. F.; Reichelt, M. W. *SIAM J. Sci. Comput.* **1997**, *18*, 1−22.
(51) Shampine, L. F.; Reichelt, M. W.; Kierzenka, J. A. *SIAM Rev.* **1999**, *41*, 538−552.
(52) Chang, J. S.; Cooper, G. *J. Comput. Phys.* **1970**, *6*, 1−16.
(53) Rempel, J. Y. *Insights into Formation of Semiconductor Nanocrystals: From First Principles Calculations to Kinetic Models of Nucleation and Growth*; MIT: Cambridge, MA, 2008.
(54) Rhee, H.-K.; Aris, R.; Amundson, N. R. *First-Order Partial Differential Equations: Theory and Application of Single Equations*; Dover Publications: Mineola, NY, 1986.
(55) Hänggi, P.; Grabert, H.; Talkner, P.; Thomas, H. *Phys. Rev. A* **1984**, *29*, 371−378.
(56) Shizgal, B.; Barrett, J. C. *J. Chem. Phys.* **1989**, *91*, 6505−6518.
(57) Wu, D. T. *Solid State Phys.* **1996**, *50*, 37−187.